Composites Part B 215 (2021) 108796

Contents lists available at ScienceDirect

Composites Part B

journal homepage: www.elsevier.com/locate/composites

Influence of elastomeric matrix and particle volume fraction on the mechanical response of magneto-active polymers

D. Garcia-Gonzalez [a,*], M.A. Moreno [a], L. Valencia [b], A. Arias [a], D. Velasco [b,c]

[a] Department of Continuum Mechanics and Structural Analysis, Universidad Carlos III de Madrid, Avda. de la Universidad 30, 28911 Leganés, Madrid, Spain
[b] Department of Bioengineering and Aerospace Engineering, Universidad Carlos III de Madrid, Avda. de la Universidad 30, 28911 Leganés, Madrid, Spain
[c] Instituto de Investigacion Sanitaria Gregorio Marañon, Madrid, Spain

ARTICLE INFO

Keywords:
Magneto-active polymer (MAP)
Mechanical characterisation
Constitutive modelling
Multifunctional composites
Magneto-mechanics
Crosslinking

ABSTRACT

Magneto-active polymers (MAPs) are revolutionising the fields of material science and solid mechanics as well as having an important presence in the bioengineering community. These composites consist of a polymeric matrix (i.e., elastomer) filled with magnetic particles (i.e., iron particles). When bonded together, these two phases form a continuum solid that, under the application of an external magnetic field, mechanically reacts leading to changes in shape and volume or/and alterations in its rheological properties. Such a magneto-mechanical response is determined by the material properties of the polymeric matrix and magnetic particles. In this work, we present the mechanical characterisation of MAPs constituted by PDMS filled with carbonyl iron powder (CIP) particles. To this end, sixteen different combinations of elastomeric base/crosslinker mixing ratio (from 5:1 to 20:1) and particles' volume fraction (from 0% to 30%) are tested under tensile loading. These results are analysed and provide the bases for the formulation of a nonlinear constitutive model that accounts for these dependencies. The modelling approach is extended to incorporate magneto-mechanical effects. Finally, the complete model is used to provide theoretical guidance for magneto-active systems, highlighting potential applications in epithelial wound healing stimulation.

1. Introduction

Magneto-active polymers (MAPs) are smart materials which modify their mechanical properties in response to their surrounding conditions. They count on dispersed nano- or micrometre iron particles (typically 1–5 μm) fixed within the polymeric matrix which lends a magnetostrictive response [1,2]. The position of such particles is that in which they remain during the curing process, where a magnetic field can be applied to force anisotropy (see [3] for review). Since rheological properties are tuned with the application of a magnetic field, MAPs have state-of-the-art applications in mechanical damping systems, soft-robotics, valves, seismic isolators, tactile displays and anti-impact devices [1,4–10]. Biological applications are currently gathering scientist's interest in these multifunctional materials. Peristaltic pumps [11], and even more sophisticated uses such as potential wound healing stimulation, are examples of MAPs' potential in biomedicine. The latter is quite promising as it would promote cellular proliferation and migration stimulation according to what needed [12].

Magneto-rheological elastomers (MREs) display strong nonlinear interaction between the magnetic particles and the elastomeric matrix [13]. The preparation of the MAP undergoes a curing procedure to stiffen the PDMS. The PDMS and the crosslinker, usually a platinum catalyst [14], are put together in such a way that the matrix chains increase their crosslinking degree. It is vital to eliminate gas bubbles in order to avoid cavitation issues (see Section 2 for more detail). The magnetic particles' volume fraction is limited up to approximately 40 % by the percolation threshold [15]. Moreover, it is common to incorporate additives (i.e. plasticisers) to improve mechanical interactions between the matrix and dispersed phase [16]. If no external magnetic field is applied during the curing process, the resulting material is isotropic [17,18]. However, if an external magnetic field is applied during curing, the particles migrate reaching for the lowest energy state. A preferred-direction of the particles aligned with the field would make the MAP mechanically stiffer along such a direction [1]. It has been widely reported that adding magnetic particles, either iron- or carbon-based, helps at tuning the composite mechanical properties [4,19]. For applications in intelligent sensors, wearable devices and soft robotics, the MAP may display anisotropic piezoconductive properties. Anisotropic liquid metal-filled magnetorheological elastomers (ALMMRE) incorporate liquid metal microdroplets, together with the magnetic solid particles, to achieve a higher electrical conductivity.

* Corresponding author.
E-mail address: danigarc@ing.uc3m.es (D. Garcia-Gonzalez).

https://doi.org/10.1016/j.compositesb.2021.108796
Received 17 January 2021; Received in revised form 22 February 2021; Accepted 11 March 2021
Available online 16 March 2021

Besides, they can adjust their electrical resistance depending on their deformation state and orientation. Yun et al. [20] designed and studied an ALMMRE with improved electrical conductivity applying a magnetic field to get the magnetic particles aligned with the metal liquid droplets, thus reducing the distance between them. In addition, the amount of crosslinker plays an essential role as it tunes the mechanical properties of the matrix, as well as the effective magneto-mechanical interaction between the particles [21]. The higher the crosslinker ratio, the fewer the sedimentation problems the material encounters [15], i.e., each particle is stronger kept in its position and prevented from motion. Related to this latter issue, curing temperature must be high enough to ensure a sufficiently quick process with no time for particles to sediment. Khanafer and Pelteret suggest temperatures of 65 and 75 °C for 12 and 16 h, respectively [15,21]. A faster curing procedure of 1 h is proposed by Wang for PDMS [22]. Recently, there have been reported new approaches to improve the mechanical properties of MAPs via acting on the matrix. Shu et al. [23] proposed to constrain the mobility of polymeric chains by bonding 3D-printed layers of a flax fibre reinforcement to the matrix. This, together with the reinforcing effect of magnetic particle chains and the vulcanised matrix, gives a higher performance MRE (i.e., increase in the shear storage modulus from 1.1 to 2.3 MPa for four layers of flax fibre). These composites are extremely suitable for light-weighted and high-strengthened 3D scaffolds.

When mechanically responding to magnetic fields, different multi-physical couplings occur within the MAP. In this regard, an external magnetic field interacts with the magnetic particles creating internal forces in the composite. Furthermore, depending on the relative magnetic permeability of the particles, their movement due to mechanical deformation also alters the magnetic fields. To help at conceptualising these magneto-active systems and guiding their design, theoretical models are formulated describing the magneto-mechanical physics of MAPs. These approaches are usually developed on macroscopic invariant-based [24,25] or on microstructural based formulations [26–29]. The former predicts well the overall material behaviour even though sometimes fails at explaining the underlying physics. One of the first works was done by Brigadnov and Dorfmann [30]. The latter, in contrast to phenomenological models, considers microstructural features of the MAP. One of the first approaches is due to Jolly et al. [17], who developed a lattice model accounting for the relative position of the magnetic particles within the polymeric matrix. A distinctive feature of a good constitutive model is to be able to incorporate the physics with just a few parameters. In this regard, the use of semi-physical microstructural models, i.e., macroscopic formulations accounting for microstructural features, outstands as ideal candidates to accomplish efficient approaches with direct links to the MAP physics [28,31].

In this work, we present the mechanical characterisation of MAPs constituted by PDMS filled with carbonyl iron powder (CIP) particles. The mechanical behaviour of the MAP is studied by uniaxial tensile loading through sixteen manufacturing configurations, combining different crosslinker mixing ratios (from 5:1 to 20:1) and magnetic particles' volume fraction (from 0% to 30%). These results are first used to calibrate a hyperelastic model (eight-chain based model) against each stress–strain curve by making use of an optimisation algorithm (without any physical constraint at this stage). Then, the calibrated model parameters along with the physical interpretation of the experimental results are used to motivate a unified formulation to describe the nonlinear response of the MAPs tested depending on the manufacturing conditions. The parameters of this model are found by using an optimisation algorithm, this time imposing physically-motivated constraints in the calibration process. Afterwards, the modelling approach is extended to incorporate magneto-mechanical response. The effects of an external magnetic field applied on the material are analysed by means of shear modulus changes depending on the manufacturing conditions of the MAP. Finally, these numerical results are used to provide theoretical guidance for magneto-active systems, highlighting potential applications in wound healing stimulation and other cellular development processes.

2. Experimental characterisation

This section introduces the materials and methods used to manufacture and to experimentally characterise the MAP samples, as well as the experimental results.

2.1. Material and manufacturing method

The main output of this section is to provide the mechanical properties of MAP samples composed of an elastomeric matrix filled with magnetic particles. More concretely, we aim at providing the influence of two main manufacturing features on the mechanical performance of the composite under tensile loading. To this end, the baseline materials chosen are:

- An elastomeric, PDMS, component for the matrix phase. PDMS is widely used in bioengineering applications in the form of cellular substrate, stencil, and others [32–35]. With an appropriate coating, it allows for cellular proliferation and migration while presenting mechanical properties close to different cellular environments or extracellular matrices (i.e., in skin or epithelial systems). In addition, it is commercially available and allows for a quite wide range of stiffness properties depending on the crosslinker amount (or mixing ratio used). This point is very interesting in mechanobiological applications where stiffness gradients play a very relevant role (i.e., cellular proliferation, cellular migration, cellular differentiation). This PDMS network consists of a Sylgard 184 silicone elastomer base and a curing agent manufactured by Dow Corning. These two components are mixed at different base/curing agent mass ratios (hereafter referred to as mixing ratio) considering: 5:1; 10:1; 15:1; and 20:1. This mixing ratio can be alternatively expressed as crosslinker amount (cl_a) following the relation: $cl_a = 0.2$ for 5:1; $cl_a = 0.1$ for 10:1; $cl_a = 0.07$ for 15:1; and $cl_a = 0.05$ for 20:1.
- Magnetic particles consisting of carbonil iron powder (CIP) from BASF company (technical denomination: soft SQ CIP) with an average diameter of 3.9–5.0 μm. These particles are added to the elastomeric matrix at different particles' volume ratios (ϕ): 0%; 5%; 15%; and 30%.

Thus, the experimental campaign considers a total number of sixteen different manufacturing conditions as a result of all the possible combinations between the mixing ratios (cl_a) and particles' volume fraction (ϕ) presented. The samples are prepared following the dog-bone shape specimens with the geometry (ASTM standards) given in Barba et al. [36]. For this purpose, a mechanised mould was used for the fabrication of the specimens providing good temperature resistance during the curing process. For the manufacturing process, the elastomer base and curing agent are firstly mixed at the given mixing ratio. Then, the magnetic particles are added at the given volume ratio according to the expression

$$m_p = \frac{m_m \phi \rho_p}{(1-\phi)\,\rho_m} \tag{1}$$

where m_p and m_m are the particles and elastomeric matrix masses, ϕ is the CIP volume ratio, $\rho_p = 7874$ kg/m^3 and $\rho_m = 982$ kg/m^3 are the particles and elastomeric matrix densities. Note that this expression is directly derived considering $\phi = V_p/(V_m + V_p)$ and $V_i = \rho_i m_i$, where V_p and V_m are the volume of the particles and matrix, respectively.

After mixing of the PDMS and CIP components, the mixture is placed under vacuum for 20 min to remove air bubbles. Finally, the composite is cured in an oven at 70 °C for 2 h. No external magnetic field is applied during curing so that isotropic distribution of the particles is reached. Note that this manufacturing protocol was chosen from various alternatives tested (changing the manufacturing times and the curing temperature) as it showed the best repeatability from the conditions tested.

2.2. Mechanical uniaxial tensile tests

This section studies the macroscopic mechanical response of PDMS-CIP magneto-active composites under mechanical tensile loading. These manufactured MAPs are tested in the form of dog-bone shape specimens [36] under uniaxial tensile deformation. The tests were conducted using a universal machine with a 1 kN load cell and at a strain rate of 0.01 s^{-1}. A total number of sixteen different manufacturing conditions combining mixing ratios of $cl_a = \{0.2, 0.1, 0.07, 0.05\}$ and particles' volume fraction of $\phi = \{0, 0.05, 0.15, 0.3\}$ are tested, conducting four tests per sample configuration (with a total of 64 experiments). Thus, the influence of these manufacturing conditions on the mechanical response of the MAP can be elucidated.

The mean experimental results for the different conditions tested, by means of true stress–true strain curves, are presented in Fig. 1. Note that these curves represent the average mechanical response from four tests on different samples per condition. The results are quite repeatable with a maximum error, in terms of Young's modulus, less than 5.8%. Note that we refer here to Young's modulus as the initial slope of the true stress–true strain curve, although the response of the material is highly nonlinear. The repeatability by means of strain at failure was not that good, with a maximum error of 17.3%. Note that this mechanical property is much more susceptible to material defects. However, in this work we do not focus on failure but on stiffness and nonlinear mechanical response. Next, a more detailed analysis of the experimental results is presented along with a discussion on the influence of mixing ratio and particles' volume fraction.

2.3. Discussion on mechanical characterisation tests

The results presented in Fig. 1 show relevant tendencies in the mechanical response of the PDMS-CIP MAPs. To provide a suitable context for comparison between configurations tested, the set of results for each mixing ratio are highlighted in different colours with the remaining tests in the background (grey lines). When fixing the mixing ratio and changing the particles' volume fraction, the same qualitative trend is appreciated. All MAP configurations have a quasi-linear regime in the first deformation region and, then, it becomes highly nonlinear at larger strains. This nonlinearity is associated to the stretchability of the molecular chains that form the polymeric network. The effect of increasing particles' volume fraction is clearly noted as an increase in overall stiffness (along the whole stress–strain response) for all the mixing ratios tested. However, this stiffening effect is slightly different depending on the mixing ratio used. In this regard, it seems that the stiffer the elastomeric matrix, the higher the influence of particles' volume ratio. This may be explained by the fact that, under tensile loading, the stresses within the MAP are transmitted by the polymeric network, serving this as vehicle to connect the magnetic particles (a priori disconnected between them). Then, when the composite is stretched, the deformation is concentrated within the softer phase and, therefore, the softer the polymeric network, the smaller the particles' contribution to mechanical stress.

Moreover, the mixing ratio used to manufacture the elastomeric matrix also has a very relevant role on the mechanical performance of the MAP. When analysing the experimental results, no relationship between the mixing ratio and the material stiffness can straightforwardly be identified. The MAP presents an increase in stiffness with crosslinker amount until $cl_a = 0.1$ (i.e., mixing ratio 10:1) but, from this point, the MAP stiffness decreases for higher crosslinker amount (i.e., $cl_a = 0.2$). A quantitative analysis on the influence of crosslinker amount is provided by means of stress evaluated at a strain of 0.6 for 0% of particles' volume fraction: (a) 1.08 MPa for 5:1, (b) 1.50 MPa for 10:1, (c) 0.35 MPa for 15:1, (d) 0.33 MPa for 20:1. In the literature, previous works have tackled the study of the effect of mixing ratio on the mechanical behaviour of PDMS (without particles' reinforcement). Wang et al. [22] studied the effect of mixing ratio on the mechanical response of PDMS under uniaxial compressive loading for a range from 5:1 to 33:1. These authors obtained a linear relationship between crosslinker amount and Young's modulus for the whole range. However, in another article, Khanafer et al. [21] observed a nonlinear relationship between Young's modulus and crosslinker amount, this time under tensile loading for a range of mixing ratio from 6:1 to 10:1. The latter work showed a nonlinear tendency consistent with the original results reported here. This tendency may be explained by the effect of crosslinker amount on the resultant crosslinking after curing. This is schematised in Fig. 2. Earlier studies on PDMS elastomers attributed the decrease in stiffness at high crosslinker amounts to the imperfection induced by an unbalanced stoichiometry between the elastomeric precursor and the crosslinker. In this regard, higher concentrations of the curing agent can result in network dilution or voids, thus impacting the final crosslinking degree [37–39].

3. Constitutive modelling

This section addresses the constitutive formulation to define the mechanical response of the (PDMS-CIP) MAPs tested previously. Under tensile loading, most of the mechanical deformation is experienced by the polymeric matrix. This fact results in an overall deformation of the composite within the finite (large) strain regime. In the following, based on a definition of the problem for finite deformations, we introduce two different approaches: first, we make use of a microstructural-based model to describe the mechanical behaviour of each MAP configuration tested; and, secondly, we propose a unified formulation to account for polymeric mixing ratio and particles' volume fraction.

3.1. Constitutive model for PDMS based MAPs

Here, we use a formulation based on the eight-chain model proposed by Arruda and Boyce [40]. This formulation is employed independently for the different mixing ratio and particles' volume fraction combinations, thus leading to sets of model parameters for each MAP configuration.

3.1.1. Formulation

Due to the considerably high deformability of the MAP, we need to differentiate between the material configuration $\mathcal{B}_0$ and the spatial configuration $\mathcal{B}_t$. Thus, a deformable body presents material coordinates $\boldsymbol{X}$ in $\mathcal{B}_0$ and, once deformed, it moves onto the spatial coordinates $\boldsymbol{x}$ in $\mathcal{B}_t$. This transformation is determined by a nonlinear deformation map χ. This concept leads to the definition of the deformation gradient $\boldsymbol{F}$, and its Jacobian J, as

$$\boldsymbol{F} = \text{Grad } \chi; \quad J := \det \boldsymbol{F} > 0. \tag{2}$$

Based on this deformation gradient, other relevant strain measures can be defined as

$$\boldsymbol{b} := \boldsymbol{F}\boldsymbol{F}^T, \quad \boldsymbol{C} := \boldsymbol{F}^T\boldsymbol{F} \tag{3}$$

where $\boldsymbol{b}$ and $\boldsymbol{C}$ are, respectively, the left and the right Cauchy–Green tensors.

Considering isothermal and quasistatic conditions, the mechanical contribution to the strain energy function (per unit reference volume) of the MAP composite can be defined by means of the deformation gradient ($\boldsymbol{F}$) as

$$\Psi_{mech} = \tilde{\Psi}_{mech}(\boldsymbol{F}). \tag{4}$$

Making use of this definition along with thermodynamics principles, a consistent derivation of the stress tensor can be obtained as (see previous works for more details [28])

$$\boldsymbol{P}_{mech} = -p\boldsymbol{F}^{-T} + \frac{\partial \Psi_{mech}}{\partial \boldsymbol{F}} \tag{5}$$

where $\boldsymbol{P}_{mech}$ is the mechanical first Piola–Kirchhoff stress tensor and the first term in the right-hand side is added to account for volumetric

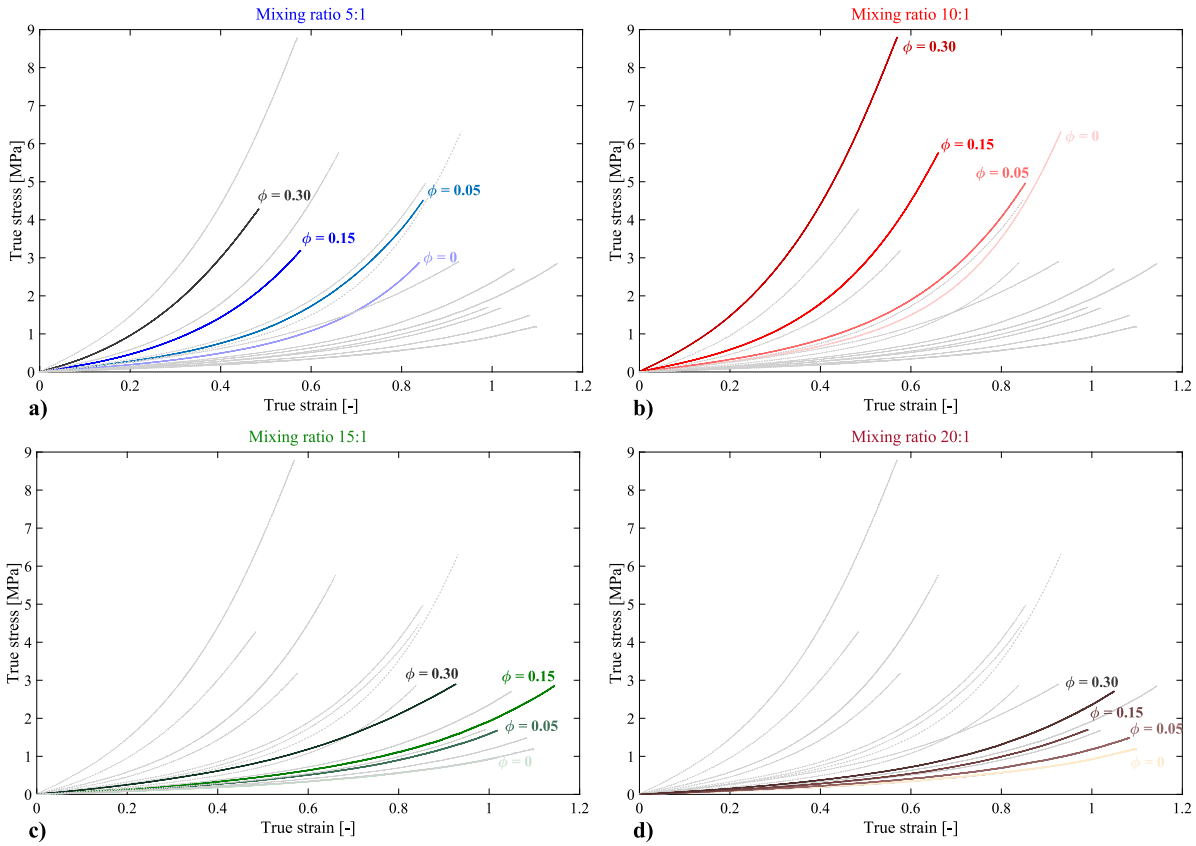

Fig. 1. Experimental results of the uniaxial tensile tests performed for different MAP configurations combining particles' volume fractions $\phi = \{0, 0.05, 0.15, 0.3\}$ and mixing ratios of: (a) 5:1, (b) 10:1, (c) 15:1, (d) 20:1. Note that, to provide a better comparison context, the set of results is highlighted in different colours with the remaining tests in the background (grey lines). (For interpretation of the references to colour in this figure legend, the reader is referred to the web version of this article.)

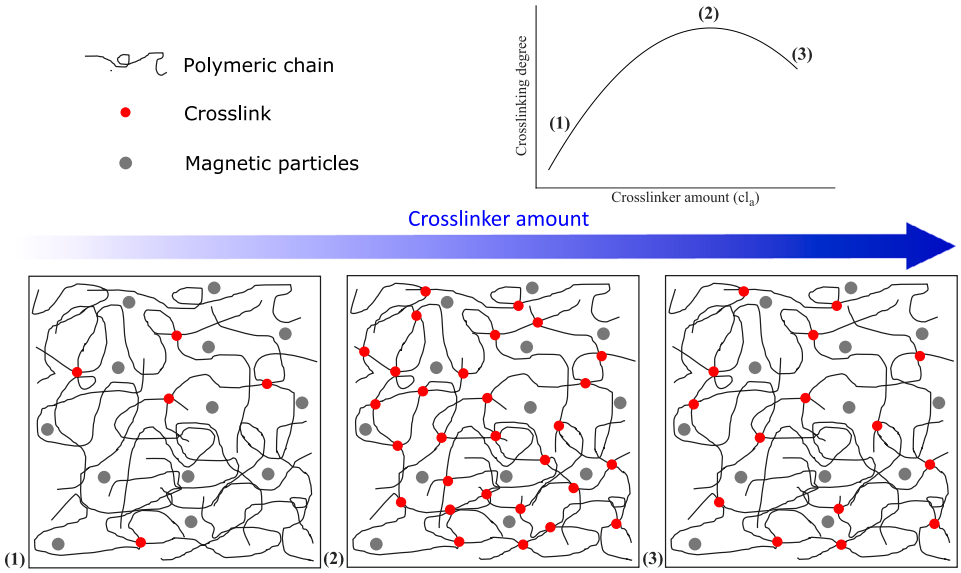

Fig. 2. A schematic diagram of the effect of crosslinker amount (cl_a) on the crosslinking degree and, consequently, on the final microstructure of the elastomeric matrix of the MAP. In the diagram, the polymeric chains are presented as blue solid lines, the crosslinks as red dots and the magnetic particles as grey dots. (For interpretation of the references to colour in this figure legend, the reader is referred to the web version of this article.)

contribution under incompressible material deformation. In this regard, p is a Lagrange multiplier associated with the volumetric pressure.

This stress tensor can be alternatively expressed in the form of Cauchy stress $\boldsymbol{\sigma}_{mech}$ (represented in the spatial configuration) as

$$\boldsymbol{\sigma}_{mech} = \boldsymbol{J}^{-1}\boldsymbol{P}_{mech}\boldsymbol{F}^{T}. \tag{6}$$

The experimental results observed in Fig. 1 and their physical interpretation discussed in Fig. 2, suggest direct links between microstructural features of the MAP and the macroscopic mechanical response. Therefore, the present modelling problem seems very suitable to be tackled by microstructural-based approaches. Among different existing models in the literature, the eight-chain model proposed by Arruda and

Boyce [40] stands out as a very well-established and accepted approach. This consists in a hyperelastic formulation that is physically motivated by deformation mechanisms of elastomers (such as the polymeric matrix used in this work). The model assumes chain molecules that, on average, are located along the diagonals of a unit cell. Thus, the probability distribution of the end-to-end distance of the molecular chains can be expressed by using the inverse of the Langevin function as

$$\Psi_{mech}(\boldsymbol{F}) = n_e k_B \theta \sum_{k=1}^{K} \frac{C_k}{N_e^{k-1}} \left[I_1^k - 3^k \right] \tag{7}$$

where n_e is the number of chains per reference volume, k_B is the Boltzmann's constant, θ is the temperature (in this work assumed constant and equal to room temperature, 296 K), and N_e is the number of Kuhn segments per polymer chain. $I_1 = \mathrm{tr}(\boldsymbol{C})$ is the first invariant of the right Cauchy–Green deformation tensor. Note that here, the inverse of the Langevin function has been approached taking up to five terms in the Padé approximation, i.e., $\left[C_1, C_2, C_3, C_4, C_5\right] = \left[\frac{1}{2}, \frac{1}{20}, \frac{11}{1050}, \frac{19}{7000}, \frac{519}{673750}\right]$.

Finally, the free energy presented in Eq. (7) can be consistently derived following Eq. (5) so that the mechanical stress reads as

$$\boldsymbol{P}_{mech} = -p\boldsymbol{F}^{-T} + \left[2 n_e k_B \theta \sum_{k=1}^{K} \frac{k C_k}{N_e^{k-1}} I_1^{k-1} \right] \boldsymbol{F}. \tag{8}$$

3.1.2. Numerical results and discussion

At this stage, each mean experimental curve, representing a specific combination of mixing ratio and particles' volume fraction, has been analysed individually. For that, we have calibrated the constitutive equation (Eq. (8)) for each curve presented in Fig. 1. To this end, we have used an optimisation algorithm implemented in an own code without imposing any physical constraint in the process. This algorithm simply searches for the best combination of parameters $\{n_e, N_e\}$ that minimises the error between the model predictive true stress–true strain curves and the experimental corresponding one. Note that the predicted true stress data from the model needs to transform the expression given in Eq. (8) with the relation given in Eq. (6) to provide the Cauchy stress tensor.

The final calibrated parameters for each condition are given in Table 1. The corresponding model predictions along with the experimental data are presented in Fig. 3. A very good agreement between experiments and model predictions can be found for all the samples tested, indicating a good predictive capability. These results then suggest that the eight-chain model can capture the nonlinearities of the mechanical response and that the model parameters strongly depend on the mixing ratio (given by cl_a) and the particles' volume fraction (ϕ). Although no physical constraints have been imposed in the calibration process, some clear tendencies of the model parameters with both mixing ratio and particles' volume fraction can be appreciated. These trends are further analysed in the following section to, along with the discussion presented for Fig. 2, motivate a unified constitutive formulation accounting for such dependencies.

3.2. Unified formulation accounting for mixing ratio and particles' volume fraction effects

In this section, we propose a unified formulation to account for polymeric mixing ratio and particles' volume fraction in a modified version of the eight-chain model.

3.2.1. Formulation

From the analysis of the experimental results (Fig. 1), a clear dependence with particles' volume fraction can be observed, i.e., the higher the particles' volume fraction, the stiffer the mechanical response of the MAP. If the material parameters identified from the previous section are analysed, Table 1, such a tendency with particles' volume fraction (ϕ) can also be inferred. In this regard, an overall increase in chain density n_e and an overall decrease in N_e are observed when increasing ϕ. Note that the former (n_e) is directly associated with shear modulus as $\left[n_e k_B \theta\right]$ and the latter (N_e) is directly associated with the extensibility of the chains. This effect can be captured by adopting an amplification factor approach, see Alshammari et al. [41], Liao et al. [42]. To this end, the first invariant I_1 is modified as

$$I_{1,h} = X \left[I_1 - 3 \right] + 3 \tag{9}$$

where X is the application factor defined as

$$X = 1 + 0.67 g\phi + 1.62 \left[g\phi \right]^2 \tag{10}$$

with g being a factor describing the asymmetric nature of the aggregated clusters.

Moreover, a relevant effect of the mixing ratio (or crosslinker amount, cl_a) is also observed in the experimental results (Fig. 1). However, this dependence of the mechanical response of the MAP is not directly proportional as with particles' volume ratio but follows a parabolic relationship. According to the discussion presented above and some published works [21,43], the crosslinking degree of the elastomeric matrix is not linearly dependent on cl_a. Instead, it shows a parabolic relation with an optimal cl_a. Therefore, higher crosslinking is reached when increasing cl_a but, from the optimal value, if higher cl_a is used, the resulting crosslinking degree decreases (see Fig. 2). Attending to the physical interpretation of the model parameters, we establish certain physically-motivated assumptions:

- Number of polymeric chains per reference volume (n_e): this variable must directly depend on the crosslinking degree. Therefore, it must evolve with cl_a following the same tendency of crosslinking with this variable (Fig. 2).
- Number of Kuhn segments (N_e): this variable must inversely depend on the crosslinking degree. Therefore, it must evolve with cl_a following the inverse tendency of crosslinking with this variable (Fig. 2).
- Amplification parameter (g): this variable indicates the stiffening effect of adding particles on the MAP composite. In a tensile deformation process, the particles distance each other in the loading direction. These are linked by the polymeric matrix, which is the responsible for transmitting the mechanical waves and, therefore, the mechanical stress within the MAP. As the magnetic particles present a stiffness of various orders of magnitude higher than the elastomer stiffness, when decreasing the stiffness of the elastomeric matrix, the deformation is highly concentrated in this

Table 1
Constitutive parameters used in the simulations of Fig. 3. The temperature is assumed constant a equal to room temperature, i.e., θ = 296 K. The Boltzmann's constant is $k_B = 1.380648 \cdot 10^{-23}$ m^2 kg s^{-2}K^{-1}.

MAP configuration		Model parameters	
cl_a [–]	ϕ [–]	n_e [m^{-3}]	N_e [–]
0.2 (5:1)	0.00	$5.708 \cdot 10^{25}$	2.5
	0.05	$6.708 \cdot 10^{25}$	2.0
	0.15	$6.708 \cdot 10^{25}$	1.2
	0.30	$9.708 \cdot 10^{25}$	1.0
0.1 (10:1)	0.00	$6.708 \cdot 10^{25}$	2.2
	0.05	$8.944 \cdot 10^{25}$	2.3
	0.15	$1.094 \cdot 10^{26}$	1.4
	0.30	$1.994 \cdot 10^{26}$	1.2
0.07 (15:1)	0.00	$2.854 \cdot 10^{25}$	15.4
	0.05	$3.854 \cdot 10^{25}$	6.0
	0.15	$4.854 \cdot 10^{25}$	6.8
	0.30	$8.854 \cdot 10^{25}$	5.9
0.05 (20:1)	0.00	$2.854 \cdot 10^{25}$	13.3
	0.05	$2.854 \cdot 10^{25}$	6.0
	0.15	$3.850 \cdot 10^{25}$	4.9
	0.30	$5.314 \cdot 10^{25}$	5.3

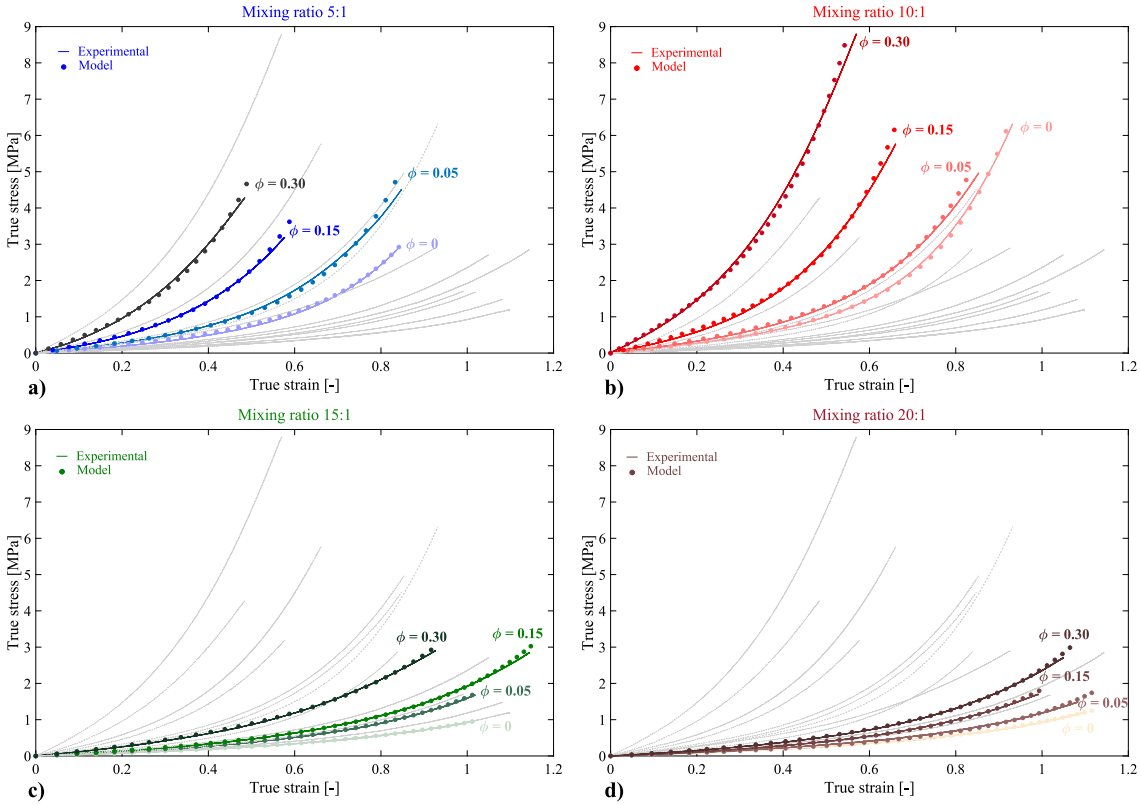

Fig. 3. Comparison of numerical predictions for the 8-chain model formulation and experimental results of the uniaxial tensile tests performed for different MAP configurations combining particles' volume fractions $\phi = \{0, 0.05, 0.15, 0.3\}$ and mixing ratios of: (a) 5:1, (b) 10:1, (c) 15:1, (d) 20:1. Note that, to provide a better comparison context, the set of results are highlighted in different colours with the remaining tests in the background (grey lines). The model parameter used in these simulations are collected in Table 1. (For interpretation of the references to colour in this figure legend, the reader is referred to the web version of this article.)

phase. In such a scenario, the stiffening effect of the particles is less pronounced. Therefore, we assume g to follow a direct relationship with n_e and, then, an equivalent similar tendency with cl_a.

These dependencies can be intuited from the model parameters identified in the previous section (Table 1), although these are not that clear. To account for these assumptions in the constitutive formulation we rewrite the model parameters as

$$n_e = \tilde{n}_e(cl_a); \quad N_e = \tilde{N}_e(cl_a); \quad g = \tilde{g}(cl_a). \tag{11}$$

Therefore, the unified mechanical contribution to the free energy becomes

$$\Psi_{mech}(\boldsymbol{F}) = \tilde{n}_e(cl_a) k_B \theta \sum_{k=1}^{K} \frac{C_k}{\left(\tilde{N}_e(cl_a)\right)^{k-1}} \left[I_{1,h}^k - 3^k\right], \tag{12}$$

the amplification factor becomes

$$X = 1 + 0.67\tilde{g}(cl_a)\phi + 1.62\left[\tilde{g}(cl_a)\phi\right]^2, \tag{13}$$

and, consistently with Eq. (5), the mechanical first Piola–Kirchhoff stress tensor becomes

$$\boldsymbol{P}_{mech} = -p\boldsymbol{F}^{-T} + \left[2X\tilde{n}_e(cl_a)k_B\theta \sum_{k=1}^{K} \frac{kC_k}{\left(\tilde{N}_e(cl_a)\right)^{k-1}} I_{1,h}^{k-1}\right] \boldsymbol{F}. \tag{14}$$

3.2.2. Numerical results and discussion

Similarly as in the previous section, we have calibrated the parameters $\{\tilde{n}_e(cl_a), \tilde{N}_e(cl_a), \tilde{g}(cl_a)\}$ by making use of an optimisation algorithm. However, in this case, we have imposed the physically-motivated constraints (i.e., direct or inverse parabolic relationship with cl_a) and minimise the error between the model predictive true stress–true strain curves and the experimental corresponding ones accounting for all curves at once. Note that, as previously done, the predicted true stress data from the model needs to transform the expression given in Eq. (14) with the relation given in Eq. (6) to provide the Cauchy stress tensor. The final calibrated functions for the model parameters, as well as their representation versus cl_a are shown in Fig. 4.

The corresponding model predictions using the unified formulation with parameters functions collected in Fig. 4 are presented, along with the experimental data, in Fig. 5. These results show that, overall, the unified formulation describes all the major tendencies observed experimentally. Thus, the model predicts the stiffening effect of particles' volume fraction and the changes in the nonlinear mechanical response with mixing ratio. The predictive capability of the unified model is worse than the eight-chain model calibrated for each mixing ratio and particles' volume fraction combination. This was expectable as the former presents fixed parameters for the sixteen different configurations. Such a predictability could be improved by increasing the order of the eight-chain model (i.e., additive summation of hyperelastic springs) or by modifying the order of the parameters' functions. However, these improvements would lead to a higher number of model parameters making the formulation more complex and hindering the motivation of the model: easily identify the effect of manufacturing conditions on the final mechanical performance of the MAP. It can be concluded that the present unified formulation allows for identifying the main interplays between magnetic particles' volume fraction, elastomer mixing ratio and mechanical features such as stiffness and nonlinear response. Therefore, it stands for a constitutive tool to guide the design of the mechanical response of MAP composites adjusting both particles' volume fraction and elastomer mixing ratio. These aspects are of great relevance as the magnetostrictive response of the MAP directly depends on the stiffness of the elastomeric matrix and the amount of magnetic particles within the composite. In this regard, the model serves to: (i) better understand the physics underlying the problem; (ii) as a

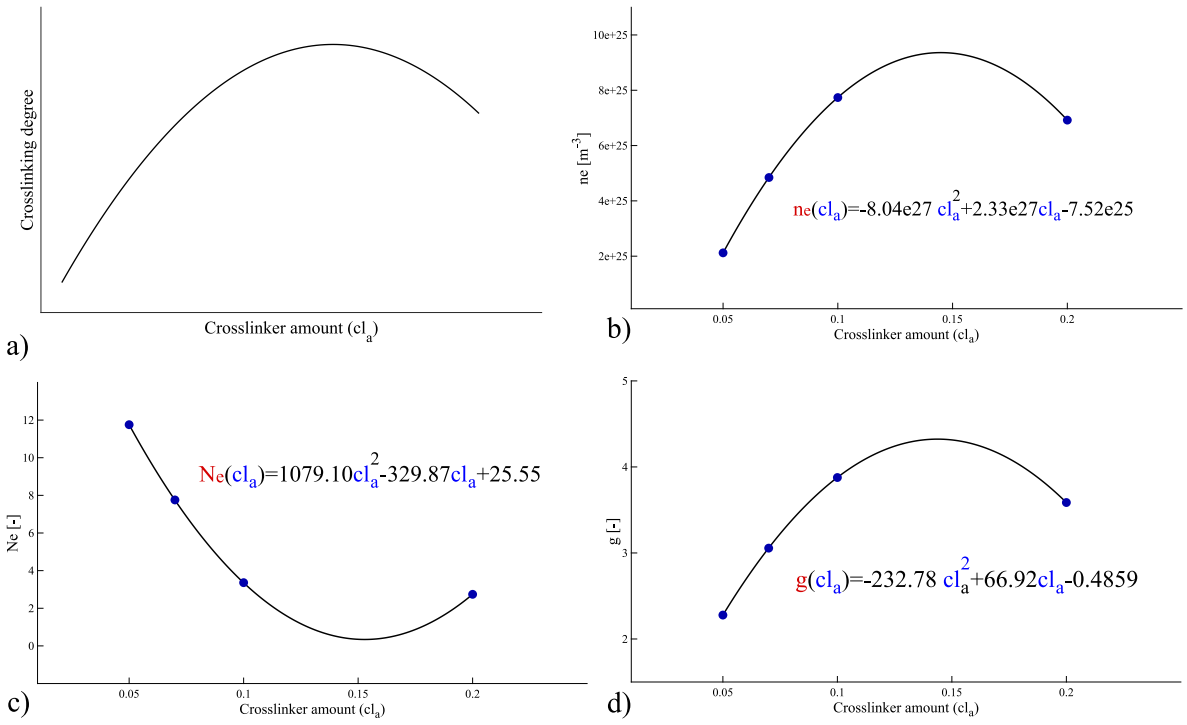

Fig. 4. (a) Effect of crosslinker amount (cl_a) on the crosslinking degree; and tendencies with corresponding expressions for: (b) ne versus cl_a; (c) Ne versus cl_a; (d) g versus cl_a. Note that these expressions are obtained on the bases of crosslinking degree-cl_a, the physical interpretation of the model parameters and the calibration against original experimental data.

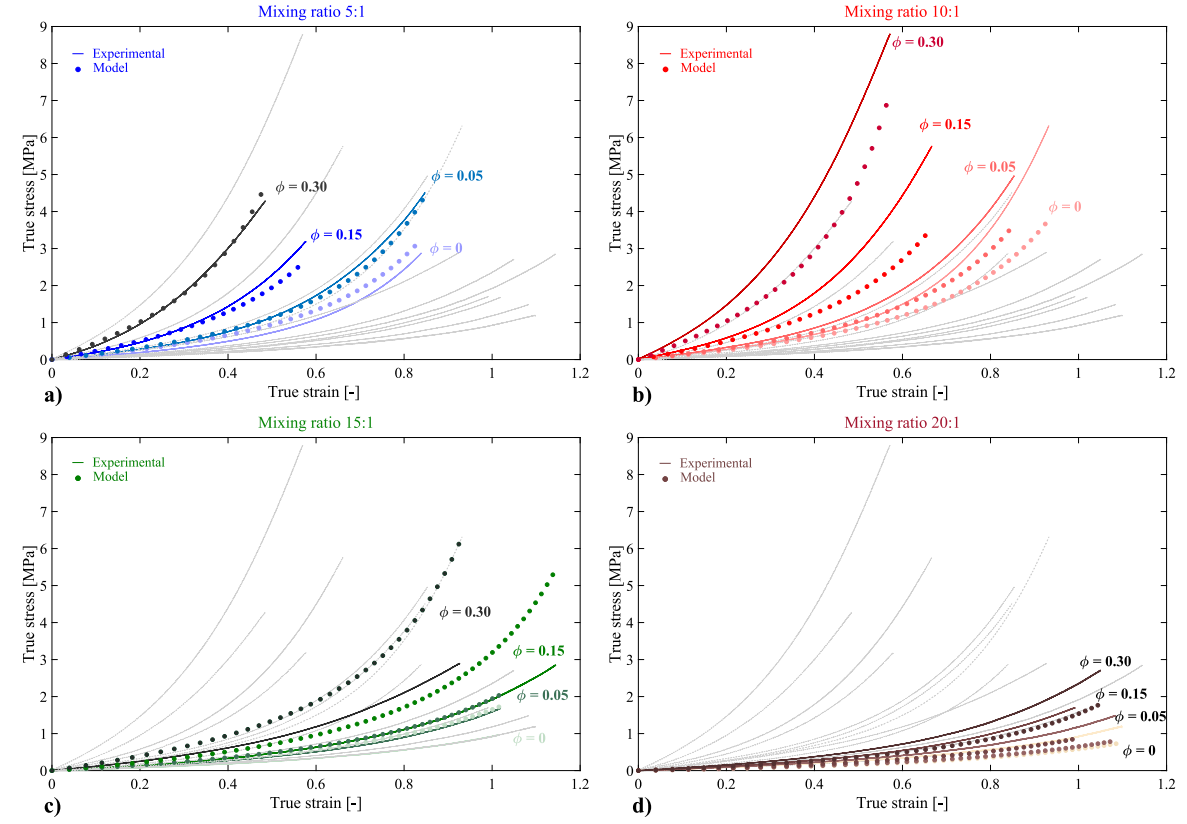

Fig. 5. Comparison of numerical predictions for the original unified formulation and experimental results of the uniaxial tensile tests performed for different MAP configurations combining particles' volume fractions $\phi = \{0, 0.05, 0.15, 0.3\}$ and mixing ratios of: (a) 5:1, (b) 10:1, (c) 15:1, (d) 20:1. Note that, to provide a better comparison context, the set of results is highlighted in different colours with the remaining tests in the background (grey lines). The model parameter used in these simulations are collected in Fig. 4. (For interpretation of the references to colour in this figure legend, the reader is referred to the web version of this article.)

numerical tool to be used in the design process of more complex structures providing a set of manufacturing conditions for each region or component.

4. Coupled magneto-mechanical formulation: predicting the effects of external magnetic fields on MAPs

This section aims at complementing the previously presented unified formulation by incorporating the magneto-mechanical response of the MAP to an external magnetic field. Under the application of such field, the CIP particles magnetise leading to dipole–dipole interactions. These interactions result into internal forces that are transmitted within the composite. As a reaction to this magnetic stress, the polymeric network deforms providing a stress contribution from the mechanical deformation of the polymeric chains. Therefore, the particles' volume fraction now plays a double role: it stiffens the mechanical response of the MAP; and it determines the magnitude of the magnetostrictive response of the MAP. Moreover, the mixing ratio still plays an important role determining the stiffness of the polymeric matrix.

4.1. Formulation

To introduce the magneto-mechanical problem, we need to define three main fundamental variables: magnetic field $\mathbb{H}$, magnetisation $\mathbb{M}$, and magnetic induction $\mathbb{B}$, expressed in the material configuration. These variables can alternatively be defined in the spatial configuration, respectively, $\mathbb{h}, \mathbb{m}$, and $\mathbb{b}$, as

$$\mathbb{H} = \mathbb{h}\boldsymbol{F}, \quad \mathbb{M} = \mathbb{m}\boldsymbol{F}, \quad \mathbb{B} = \boldsymbol{J}\mathbb{b}\boldsymbol{F}^{-T}. \tag{15}$$

These variables are related in the bulk by the constitutive definition [44,45]

$$\mathbb{B} = \boldsymbol{J}\mu_0\boldsymbol{C}^{-1}[\mathbb{H} + \mathbb{M}] \quad \text{in } \mathcal{B}_0 \tag{16}$$

where μ_0 is the magnetic permeability of the vacuum. In addition, these variables must evolve so that the magnetic balance laws given by Maxwell equations are satisfied. These laws, in their material form, read as

$$\text{Curl } \mathbb{H} = \boldsymbol{0}, \quad \text{Div } \mathbb{B} = 0, \tag{17}$$

with Curl and Div denoting the corresponding differential operators with respect to the position vectors $\boldsymbol{X}$ in $\mathcal{B}_0$.

To incorporate this physics into the constitutive formulation, we need to come back to the definition of the free energy, that now becomes (neglecting the magnetic contribution associated to the free space)

$$\Psi(\boldsymbol{F}, \mathbb{M}) = \Psi_{mech}(\boldsymbol{F}) + \Psi_{mag}(\boldsymbol{F}, \mathbb{M}). \tag{18}$$

where $\Psi_{mag}(\boldsymbol{F}, \mathbb{M})$ is the magnetic contribution to the total energy. According to this definition of the total free energy, the first Piola–Kirchhoff stress tensor is now derived as

$$\boldsymbol{P} = \boldsymbol{P}_{mech} + \boldsymbol{P}_{mag} = -p\boldsymbol{F}^{-T} + \frac{\partial \Psi_{mech}}{\partial \boldsymbol{F}} + \frac{\partial \Psi_{mag}}{\partial \boldsymbol{F}}. \tag{19}$$

For the definition of the magnetic potential we use a recently proposed formulation that is motivated by microstructural features to describe dipole–dipole interactions as (see [28] for a detailed derivation)

$$\Psi_{\text{mag}}(\boldsymbol{F}, \mathbb{M}) = -\frac{\mu_o}{4\pi}\frac{\phi^2}{\gamma}\sum_{i=1}^{N}\left[\frac{3\left[\left[\boldsymbol{F}^{-T}\mathbb{M}\right]\cdot\left[\boldsymbol{F}\boldsymbol{R}_i^0\right]\right]\left[\left[\boldsymbol{F}^{-T}\mathbb{M}\right]\cdot\left[\boldsymbol{F}\boldsymbol{R}_i^0\right]\right]}{\left\|\boldsymbol{F}\boldsymbol{R}_i^0\right\|^5} - \frac{\left[\boldsymbol{F}^{-T}\mathbb{M}\right]\cdot\left[\boldsymbol{F}^{-T}\mathbb{M}\right]}{\left\|\boldsymbol{F}\boldsymbol{R}_i^0\right\|^3}\right] \tag{20}$$

Table 2
Magnetic parameters used in the simulations of Fig. 6.

Magnetic parameters		
M_s (kA m^{-1})	μ_r (–)	μ_o (H m^{-1})
1582	21.5	$4\pi 10^{-7}$

where $\boldsymbol{R}_i^0$ represents the vectorial distance between particles in the material configuration and the dimensionless parameter γ accounts for the number of particles per representative lattice selected [see 46]. Making use of the relation presented in Eq. (19), the magnetic contribution to the stress reads as Eq. (21) in Box I.

The complete formulation still needs a constitutive relation for the magnetic problem. Similarly as done for the mechanical constitutive relation, using the definition of the total free energy along with thermodynamics principles, a consistent derivation of the magnetisation vector can be obtained as (see previous works for more details [28])

$$\mathbb{B} = \frac{\partial \Psi}{\partial \mathbb{M}}. \tag{22}$$

Finally, making use of the Legendre transform (see [28,47] for a similar approach), the magnetic constitutive relation can be written as

$$\mathbb{M} = -\frac{\partial \tilde{\Psi}}{\partial \mathbb{H}}. \tag{23}$$

Then, the Fröhlich–Kennely equation can be used to define the evolution of $\mathbb{M}$ with the magnetic field $\mathbb{H}$ as

$$\mathbb{M} = \frac{M_s\left[\mu_r - 1\right]\mathbb{H}}{M_s + \left[\mu_r - 1\right]\|\mathbb{H}\|} \tag{24}$$

with M_s being the saturation magnetisation of the magnetic particles and μ_r being the relative magnetic permeability of the particles (for more details see Refs. [46,48–50]).

4.2. Numerical results and discussion

In this section, we use the unified model formulation coupled to magneto-mechanics. In the simulations presented here, the parameters for the mechanical problem are taken from the functions presented in Fig. 4. The model parameters for the magnetic problem are collected in Table 2, which directly correspond to physical properties of CIP taken from the literature [51].

Once provided the complete formulation to predict the magneto-mechanical response of MAPs and the corresponding model parameters for the PDMS-CIP composites considered in this work, we conduct a numerical analysis on the influence of an external magnetic field on the mechanical properties of the MAP. For this purpose, we conceive a MAP sample whose mechanical boundary conditions are imposed during the whole testing process. The MAP is thus subjected to a pure shear deformation process under two different magnetic conditions: (i) null external magnetic field, i.e., $\mu_o\mathbb{H} = 0$ mT; and (ii) a constant magnetic field of $\mu_o\mathbb{H} = 200$ mT. These simulations are carried out on the different PDMS-CIP configurations by means of mixing ratio and particles' volume fraction combinations. The numerical predictions are analysed in terms of linearised shear modulus, understood as the slope of the shear component of the Cauchy stress (given by Eqs. (6) and (19)) versus the shear strain within the small deformation region. These results are collected in Fig. 6. When null external magnetic field conditions are simulated, the MAP stiffness follows the previously discussed tendencies: an increase with the particles' volume ratio ϕ and an increase with crosslinking, in turn defined by the crosslinker amount following the relation given in 4. Moreover, when an external magnetic field is applied, the magnetic particles magnetise leading to internal forces due to dipole–dipole interactions. These result in a magnetic resistance to deform in shear mode, thus stiffening the macroscopic response of the MAP composite. As inferred from Eq. (21), this

$$\boldsymbol{P}_{mag} = -\frac{\mu_o}{4\pi}\frac{\phi^2}{\gamma}\sum_i \left[\frac{-6\left(\left(\boldsymbol{F}^{-T}\mathbb{M}\right)\otimes\left(\boldsymbol{F}^{-T}\boldsymbol{F}\boldsymbol{R}_i^0\right)\right)\left(\left(\boldsymbol{F}^{-T}\mathbb{M}\right)\cdot\left(\boldsymbol{F}\boldsymbol{R}_i^0\right)\right) + 6\left(\left(\boldsymbol{F}^{-T}\mathbb{M}\right)\cdot\left(\boldsymbol{F}\boldsymbol{R}_i^0\right)\right)\left(\left(\boldsymbol{F}^{-T}\mathbb{M}\right)\otimes\boldsymbol{R}_i^0\right)}{\left\|\boldsymbol{F}\boldsymbol{R}_i^0\right\|^5} \right. \\ \left. - \frac{15\left(\left(\boldsymbol{F}^{-T}\mathbb{M}\right)\cdot\left(\boldsymbol{F}\boldsymbol{R}_i^0\right)\right)\left(\left(\boldsymbol{F}^{-T}\mathbb{M}\right)\cdot\left(\boldsymbol{F}\boldsymbol{R}_i^0\right)\right)\left(\boldsymbol{R}_i^0\otimes\boldsymbol{R}_i^0\right)\boldsymbol{F}}{\left\|\boldsymbol{F}\boldsymbol{R}_i^0\right\|^7} + \frac{2\left(\boldsymbol{F}^{-T}\mathbb{M}\right)\otimes\left(\boldsymbol{F}^{-T}\boldsymbol{F}^{-T}\mathbb{M}\right)}{\left\|\boldsymbol{F}\boldsymbol{R}_i^0\right\|^3} - \frac{3\left(\left(\boldsymbol{F}^{-T}\mathbb{M}\right)\cdot\left(\boldsymbol{F}^{-T}\mathbb{M}\right)\right)\left(\boldsymbol{R}_i^0\otimes\boldsymbol{R}_i^0\right)\boldsymbol{F}}{\left\|\boldsymbol{F}\boldsymbol{R}_i^0\right\|^5} \right] \tag{21}$$

Box I.

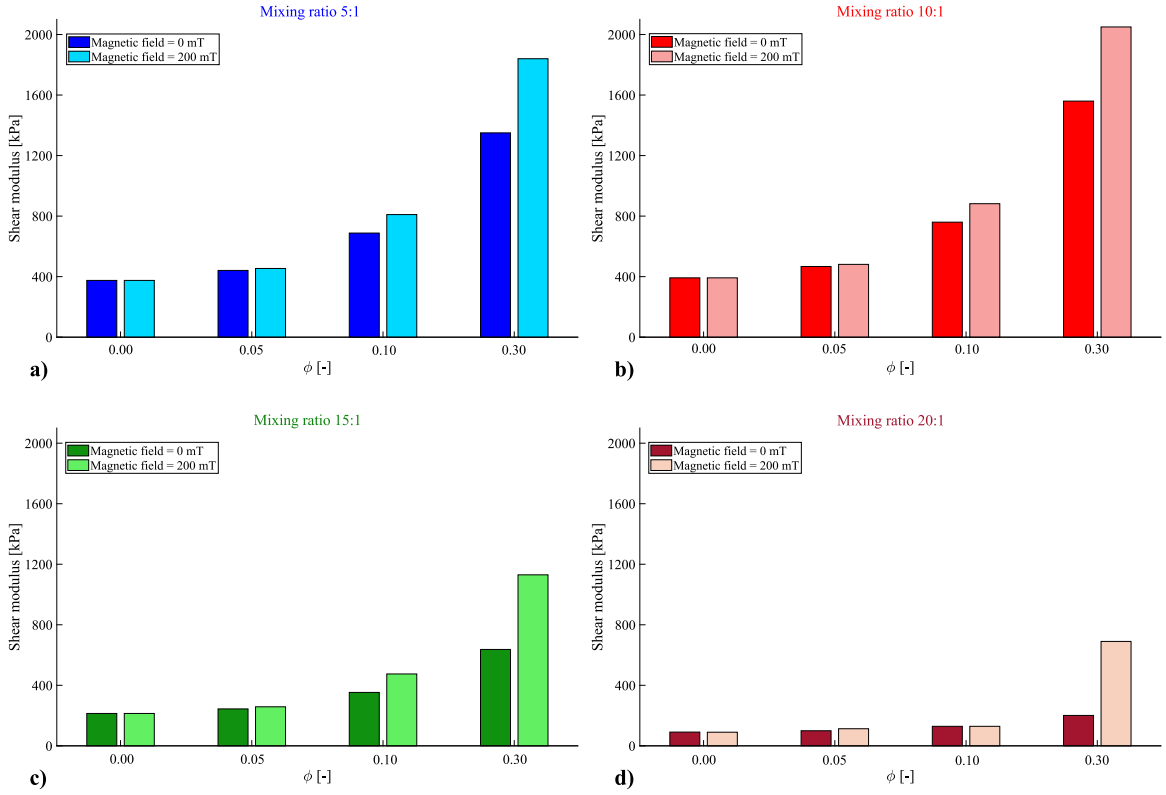

Fig. 6. Numerical predictions, using the original unified formulation, of the effective shear modulus depending on the external magnetic field for different MAP configurations combining particles' volume fractions $\phi = \{0, 0.05, 0.15, 0.3\}$ and mixing ratios of: (a) 5:1, (b) 10:1, (c) 15:1, (d) 20:1. Two magnetic fields are considered: $\mu_o\mathbb{H} = 0$ mT and $\mu_o\mathbb{H} = 200$ mT. The model parameter used in these simulations are collected in Fig. 4 and Table 2.

magnetic contribution directly depends on the particles' volume ratio. Therefore, the effect of the magnetic field on the mechanical properties of the MAP is more relevant for the higher particles' volume fraction tested. Furthermore, the relative mechanical changes expressed by the MAP due to the magnetic field also depend on the mixing ratio. In this regard, MAP configurations with lower stiffness (i.e., lower $n_e(cl_a)$) present a higher magnetostrictive response. Moreover, although in this work we focus on isotropic distributions of the magnetic particles, it is worth mentioning that the magnetorheological response of the MAP is highly dependent not only on the particles' volume ratio but also on their spatial distribution. These effects have been studied in other works (experimental characterisation, modelling and novel applications) and show higher magnetostrictive effect when the particles are aligned in a preferred orientation (forming chain like orientations) [28,52–55]. In addition, in a recent theoretical work, a transition from compression to expansion of the MAP under the application of an external magnetic field is observed depending on the microstructural arrangement of the particles [28].

Overall, the experimental work presented along with these simulations suggest different uses of MAPs for potential biological applications. For instance, wound healing processes are mainly governed by collective cell migration [56]. These processes are highly complex as they involve different physico-chemical cues. Among them, the mechanics of not only the cellular system but also of the surrounding environment, plays a major role [57]. A especially relevant process consists in the influence of heterogeneous stiffness within the cellular substrate. Such a heterogeneous substrate leads to heterogeneous external mechanical forces acting on the cell continuum [58]. As a consequence, the cellular system trends to migrate towards the stiffer regions [12,59]. This effect is termed durotaxis and has been postulated to be decisive during wound healing [60]. In vivo, these epithelial cellular systems develop within skin tissue that, depending on age, gender, orientation and location can present a stiffness ranging from 30 kPa to 140 MPa [61]. According to our work, PDMS-CIP composites, depending on the manufacturing conditions (i.e., mixing ratio and particles' volume fraction) can present a stiffness from 100 kPa to 1.6 MPa. This range is representative of the stiffness shown by skin

tissue from forearm or forehead, among others [61]. Therefore, these MAPs are great candidates as cellular substrates for in vitro testing or further applications that require a good material-skin interphase match. In addition, the presence of magnetic particles allows for controlling alterations of the mechanical properties of the substrate via application of an external magnetic field, thus promoting changes in the dynamics of cellular migration. This concept can also be extended to other biological problems such as cancer proliferation and migration [62].

5. Conclusions

This work presents the mechanical characterisation of magneto-active polymers (MAPs) composed of a PDMS matrix and carbonyl iron powder (CIP) particles. The experiments consist in uniaxial tensile tests on sixteen different manufacturing configurations combining crosslinker mixing ratios (from 5:1 to 20:1) and magnetic particles' volume fraction (from 0% to 30%). The experimental results show a direct relationship between particles' volume fraction and MAP stiffness, increasing the latter with the former. Moreover, the mixing ratio is found as a key variable determining the mechanical response of the MAP, via modulating the crosslinking degree of the polymeric matrix. In this regard, a relationship between mixing ratio and MAP stiffness is identified following a parabolic fashion.

These experimental data are numerically approached by a hyperelastic model (eight-chain based model). To this end, the experimental results are used to calibrate the model parameters against each stress–strain curve by making use of an optimisation algorithm (without any physical constraint at this stage). An almost perfect fit between experiments and model predictions is obtained from this approach. The calibrated model parameters are analysed along with the physical interpretation of the experimental results to motivate the hypotheses behind the unified formulation proposed to describe the nonlinear response of the MAPs tested depending on the manufacturing conditions. Then, we calibrate the parameters of this model making use of an optimisation algorithm, this time imposing the pertinent physically-motivated constraints during the calibration process. This unified formulation shows itself able to predict all the mechanical tendencies observed in the experiments and is afterwards extended to account for the magneto-mechanical coupling. Overall, we provide a unified formulation that, using a unique set of parameters, is able to reproduce the magneto-mechanical deformation mechanisms of MAPs. This model is formulated, within a thermodynamically consistent framework and for finite strains, on physically motivated bases providing clear links with the microstructure of both polymeric matrix and magnetic particles. To the authors' knowledge, this is the first model for magneto-active polymers accounting for all these dependencies and providing clear microstructural links. The main advantage of this model is that it allows for a formulation where both particles' volume fraction and crosslinker amount can be used as input data and it will provide the magneto-mechanical performance of the MAP. Therefore, the model serves to: (i) better understand the physics underlying the problem; (ii) as a numerical tool to be used in the design process of more complex structures providing a set of manufacturing conditions for each region or component. The magneto-mechanical model is then used to provide insights into the effects of an external magnetic field in terms of alteration of mechanical properties, i.e., shear modulus depending on the manufacturing conditions of the MAP. These numerical results show that the constitutive framework provided herein can help at conceptualising new MAPs by providing theoretical guidance on how the magneto-active systems will respond to an external magnetic field. Thus, the manufacturing conditions of the MAP composite can be controlled to provide optimal magnetorheological properties depending on the specific application. In this regard, we identify a great potential of these systems for promoting epithelial wound healing and other cellular development processes in a dynamic and remote fashion.

CRediT authorship contribution statement

D. Garcia-Gonzalez: Conceptualisation, Investigation, Experimental methodology, Numerical Methodology, Formal analysis, Writing - original draft, Writing - review & editing, Funding acquisition. **M.A. Moreno:** Investigation, Numerical methodology, Formal analysis, Writing - original draft, Writing - review & editing. **L. Valencia:** Investigation, Experimental methodology, Writing - review & editing. **A. Arias:** Investigation, Formal analysis, Writing - review & editing. **D. Velasco:** Investigation, Formal analysis, Writing - review & editing, Funding acquisition.

Declaration of competing interest

The authors declare that they have no known competing financial interests or personal relationships that could have appeared to influence the work reported in this paper.

Acknowledgements

DGG, DV and MAM acknowledge support from the European Research Council (ERC) under the European Union's Horizon 2020 research and innovation programme (grant agreement No. 947723, project: 4D-BIOMAP). The authors acknowledge support from Programa de Apoyo a la Realizacion de Proyectos Interdisciplinares de I+D para Jovenes Investigadores de la Universidad Carlos III de Madrid and Comunidad de Madrid, Spain (project: BIOMASKIN). DGG acknowledges support from the Talent Attraction grant (CM 2018 - 2018-T2/IND-9992) from the Comunidad de Madrid and MAM acknowledges support from the Ministerio de Ciencia, Innovacion y Universidades, Spain (FPU19/03874).

References

[1] Varga Z, Filipcsei G, Zrínyi M. Magnetic field sensitive functional elastomers with tuneable modulus. Polymer 2006;47:227–33.
[2] Dargahi A, Sedaghati R, Rakheja S. On the properties of magnetorheological elastomers in shear mode: Design, fabrication and characterization. Composites B 2019;159:269–83.
[3] Bastola AK, Hossain M. A review on magneto-mechanical characterizations of magnetorheological elastomers. Composites B 2020;108348.
[4] Burgaz E, Goksuzoglu M. Effects of magnetic particles and carbon black on structure and properties of magnetorheological elastomers. Polym. Test. 2020;81:0142–9418.
[5] Li Y, Li J, Tian T, Li W. A highly adjustable magnetorheological elastomer base isolator for applications of real-time adaptive control. Smart Mater Struct 2013;22(9):095020.
[6] Hu W, Zhan G, Mastrangeli M, Sitti M. Small-scale soft-bodied robot with multimodal locomotion. Nature 2018;554:81–5.
[7] Kim Y, Yuk H, Zhao R, Chester SA, Zhao X. Printing ferromagnetic domains for untethered fast-transforming soft materials. Nature 2018;558(7709):274–9.
[8] Ren Z, Hu W, Dong X, Sitti M. Multi-functional soft-bodied jellyfish-like swimming. Nature Commun 2019;10(2703).
[9] Alkhalaf A, Hooshiar A, Dargahi J. Composite magnetorheological elastomers for tactile displays: Enhanced MR-effect through bi-layer composition. Composites B 2020;190:1359–8368.
[10] Zhao C, Gong X, Wang S, Jiang W, Xuan S. Shear stiffening gels for intelligent anti-impact applications. Cell Rep Phys Sci 2020;1(12):2666–3864.
[11] Fuhrer R, Schumacher CM, Zeltner M, Stark WJ. Soft iron/silicon composite tubes for magnetic peristaltic pumping: Frequency-dependent pressure and volume flow. Adv Funct Mater 2013;23(31):3845–9.
[12] Garcia-Gonzalez D, Muñoz Barrutia A. Computational insights into the influence of substrate stiffness on collective cell migration. Extreme Mech. Lett. 2020;40:100928.
[13] Galipeau E, Ponte-Castaneda P. Giant field-induced strains in magnetoactive elastomer compo- sites. Proc. R. Soc. Lond. Ser. A Math. Phys. Eng. Sci. 2013;469:20130385.
[14] Saxena P, Pelteret JP, Steinmann P. Modelling of iron-filled magneto-active polymers with a dispersed chain-like microstructure. Eur J Mech A Solids 2015;50:132–51.
[15] Pelteret JP, Steinmann P. Magneto-active polymers: Fabrication, characterisation, modelling and simulation at the micro- and macro-scale. De Gruyter; 2020.

[16] Poojary UR, Hegde S, Gangadharan KV. Experimental investigation on the effect of carbon nanotube additive on the field-induced viscoelastic properties of magnetorheological elastomer. J. Mater. Sci. 2018;53:4229–41.

[17] Jolly MR, Carlson JD, Muñoz BC. A model of the behaviour of magnetorheological materials. Smart Mater Struct 1996;5:607–14.

[18] Boczkowska A, Awietjan SF. Smart composites of urethane elastomers with carbonyl iron. J Mater Sci 2009;44:4104–11.

[19] Perales-Martínez IA, Palacios-Pineda LM, Lozano-Sánchez LM, Martínez-Romero O, Puente-Cordova JG, Elías-Zúñiga A. Enhancement of a magnetorheological PDMS elastomer with carbonyl iron particles. Polym. Test. 2017;57:78–86.

[20] Yun G, Tang SY, Zhao Q, Zhang Y, Lu H, Yuan D, et al. Liquid metal composites with anisotropic and unconventional piezoconductivity. Matter 2020;3(3):824–41.

[21] Khanafer K, Duprey A, Schlicht M, Berguer R. Effects of strain rate, mixing ratio, and stress–strain definition on the mechanical behavior of the polydimethylsiloxane (PDMS) material as related to its biological applications. Biomed Microdevices 2009;11:503.

[22] Wang Z, Volinsky AA, Gallant ND. Crosslinking effect on polydimethylsiloxane elastic modulus measured by custom-built compression instrument. J. Appl. Polym. Sci 2014;131(41050).

[23] Shu Q, Ding L, Gong X, Hu T, Xuan S. High performance magnetorheological elastomers strengthened by perpendicularly interacted flax fiber and carbonyl iron chains. Smart Mater Struct 2020;29:025010.

[24] Lefèvre V, Danas K, Lopez-Pamies Ó. Two families of explicit models constructed from a homogenization solution for the magnetoelastic response of MREs containing iron and ferrofluid particles. Int J Non-Linear Mech 2020;119:0020–7462.

[25] Nedjar B. A modelling framework for finite strain magnetoviscoelasticity. Math Mech Solids 2020;25(2):288–304. http://dx.doi.org/10.1177/1081286519873963.

[26] Goshkoderia A, Rudykh S. Stability of magnetoactive composites with periodic microstructures undergoing finite strains in the presence of a magnetic field. Composites B 2017;128:19–29.

[27] Khanouki MA, Sedaghati R, Hemmatian M. Experimental characterization and microscale modeling of isotropic and anisotropic magnetorheological elastomers. Composites B 2019;176:1359–8368.

[28] Garcia-Gonzalez D, Hossain M. A microstructural-based approach to model magneto-viscoelastic materials at finite strains. Int J Solids Struct 2021;208–209:119–32.

[29] Zabihyan R, Mergheim J, Pelteret JP, Brands B, Steinmann P. FE2 simulations of magnetorheological elastomers: Influence of microscopic boundary conditions, microstructures and free space on the macroscopic responses of MREs. Int J Solids Struct 2020;193–194:338–56, 0020-7683.

[30] Brigadnov I, Dorfmann A. Mathematical modeling of magneto-sensitive elastomers. Int J Solids Struct 2002;40(18):4659–74.

[31] Mukherjee D, Bodelot L, Danas K. Microstructurally-guided explicit continuum models for isotropic magnetorheological elastomers with iron particles. Int. J. Non-Linear Mech. 2020;120:103380.

[32] Chuah YJ, Koh YT, Lim K, Menon NV, Wu Y, Kang Y. Simple surface engineering of polydimethylsiloxane with polydopamine for stabilized mesenchymal stem cell adhesion and multipotency. Sci Rep 2015;5(18162).

[33] Victor A, Ribeiro J, Araújo FF. Study of PDMS characterization and its applications in biomedicine: A review. J Mech Eng Biomech 2019;4:1–9.

[34] Akther F, Yakob SB, Nguyen N-T, Ta HT. Surface modification techniques for endothelial cell seeding in PDMS microfluidic devices. Biosensors 2020;10:182.

[35] Sreekantan S, Hassan M, Murthe SS, Seeni A. Biocompatibility and cytotoxicity study of polydimethylsiloxane (PDMS) and palm oil fuel ash (POFA) sustainable super-hydrophobic coating for biomedical applications. Polymers 2020;12(3034).

[36] Barba D, Arias A, Garcia-Gonzalez D. Temperature and strain rate dependences on hardening and softening behaviours in semi-crystalline polymers: Application to PEEK. Int J Solids Struct 2020;182–183:205–17.

[37] Chambon F, Winter HH. Linear viscoelasticity at the gel point of a crosslinking PDMS with imbalanced stoichiometry. J. Rheol. 1987;31:683.

[38] Wilder EA, Guo S, Lin-Gibson S, Fasolka MJ, Stafford CM. Measuring the modulus of soft polymer networks via a buckling-based metrology. Macromolecules 2006;39:4138–43.

[39] Seo J-H, Sakai K, Yui N. Adsorption state of fibronectin on poly(dimethylsiloxane) surfaces with varied stiffness can dominate adhesion density of fibroblasts. Acta Biomater 2013;9:5493–501.

[40] Arruda EM, Boyce MC. A three-dimensional constitutive model for the large stretch behavior of rubber elastic materials. J. Mech. Phys. Solids 1993;41:389–412.

[41] Alshammari BA, Al-Mubaddel FS, Karim MR, Hossain M, Al-Mutairi AS, Wilkinson AN. Addition of graphite filler to enhance electrical, morphological, thermal, and mechanical properties in 500 poly (ethylene terephthalate): Experimental characterization and material modeling. Polymers 2019;11(9):1411.

[42] Liao Z, Hossain M, Yao H. Ecoflex polymer of different shore hardnesses: Experimental investigations and constitutive modelling. Mech. Mater. 2020;144:103366.

[43] Johnston ID, McCluskey DK, Tan CKL, Tracey MC. Mechanical characterization of bulk Sylgard 184 for microfluidics and microengineering. J Micromech Microeng 2014;24:035017.

[44] Dorfmann A, Ogden RW. Nonlinear magnetoelastic deformations of elastomers. Acta Mech 2004;167(1–2):13–28.

[45] Mehnert M, Hossain M, Steinmann P. Towards a thermo-magneto-mechanical coupling framework for magneto-rheological elastomers. Int J Solids Struct 2017;128:117–32.

[46] Ivaneyko D, Toshchevikov V, Saphiannikova M, Heinrich G. Effects of particle distribution on mechanical properties of magneto-sensitive elastomers in a homogeneous magnetic field. Condens. Matter Phys. 2012;15(33601).

[47] Garcia-Gonzalez D, Landis CM. Magneto-diffusion-viscohyperelasticity for magneto-active hydrogels: Rate dependences across time scales. J Mech Phys Solids 2020;139:103934.

[48] Jiles D. Introduction to magnetism and magnetic materials. London and New York: Chapman and Hall Publishers; 1998.

[49] Bay F, Labbe V, Favennec Y, Chenot JL. A numerical model for induction heating processes coupling electromagnetism and thermomechanics. Internat J Numer Methods Engrg 2003;58:839–67.

[50] Ivaneyko D, Toshchevikov VP, Saphiannikova M, Heinrich G. Magneto-sensitive elastomers in a Homogeneous magnetic field: A regular rectangular lattice model. Macromol. Theory Simul. 2011;20:411–24.

[51] Arias JL, Gallardo V, Linares-Molinero F, Delgado AV. J. Colloid Interface Sci. 2006;299:599.

[52] Schubert G, Harrison P. Large-strain behaviour of magneto-rheological elastomers tested under uniaxial compression and tension, and pure shear deformations. Polym. Test. 2015a;42:122–34.

[53] Schubert G, Harrison P. Equi-biaxial tension tests on magneto-rheological elastomers. Smart Mater Struct 2015b;25(1):015015.

[54] Cao X, Xuan S, Li J, Li Z, Hu T, Liang H, et al. Magnetic-tunable sound absorber based on micro-perforated magnetorheological elastomer. Smart Mater Struct 2019;29:015024.

[55] Cao X, Xuan S, Hu T, Gong X. 3D printing-assistant method for magneto-active pulse pump: Experiment, simulation, and deformation theory featured. Appl Phys Lett 2020;117:241901.

[56] Alert R, Trepat X. Physical models of collective cell migration. Annu. Rev. Condens. Matter Phys. 2020;11(1):77–101.

[57] Ladoux B, Mege RM. Mechanobiology of collective cell behaviours. Nature Rev Mol Cell Biol 2017;18:743–57.

[58] Kurniawan NA, Bouten CV. Mechanobiology of the cell–matrix interplay: Catching a glimpse of complexity via minimalistic models. Extreme Mech. Lett. 2018;20:59–64.

[59] Malandrino A, Mak M, Kamm RD, Moeendarbary E. Complex mechanics of the heterogeneous extracellular matrix in cancer. Extreme Mech. Lett. 2018;21:25–34.

[60] Sunyer R, Conte V, Escribano J, Elosegui-Artola A, Labernadie A, Valon L, et al. Collective cell durotaxis emerges from long-range intercellular force transmission. Science 2016;353:1157–61.

[61] Fernandes MG, da Silva LP, Marques AP. Skin mechanobiology and biomechanics: From homeostasis to wound healing. In: Advances in biomechanics and tissue regeneration. Academic Press; 2019, p. 343–60, Chapter 17.

[62] DuChez BJ, Doyle AD, Dimitriadis EK, Yamada KM. Durotaxis by human cancer cells. Biophys J 2019;116(4):670–83.